Adopting multispectral dip components for coherence and curvature attribute computations

Satinder Chopra[1] and Kurt J. Marfurt[2]

https://doi.org/10.1190/tle39080593.1

Abstract

Although volumetric coherence is the most widely used geometric attribute, accurate estimates of volumetric dip are in some ways more important. Coherence, amplitude gradients, and gray-level co-occurrence matrix textures should be computed along structural dip. Curvature and aberrancy are computed from volumetric estimates of structural dip. Because of both differences in resolution and sensitivity to coherent noise, different frequency components may exhibit different dip. In recent years, improvements in coherence have been noticed where covariance matrices of individual spectral components are summed rather than summing the original broadband data. We extend the same concepts to compute multispectral dip estimates by using a gradient structure tensor algorithm. The results are sharper, less smeared images on the dip components. The higher-resolution dip estimates result in higher-resolution curvature and aberrancy estimates. Availability of sharper estimates of dip to guide coherence attribute results in more continuous, less noisy discontinuities.

Introduction

Frequently, we notice that conventional broadband seismic data do not necessarily provide the best insight into the interpretation of subsurface structure and stratigraphy or for the evaluation of derived seismic attributes. For example, geologic discontinuities exhibit different seismic expressions due to their intrinsic scales and can be seen better at a specific frequency range. Hardage (2009) notes that the signal-to-noise ratio in a west Texas survey depends not only on the noise spectrum, but also on target size, depth, thickness, and impedance properties. He finds faults to be better delineated by lower-frequency components than by interbed multiple contaminated broadband data. Gao (2013) also recognizes that seismic amplitude is a combination of responses to geologic features with different scales. In contrast to Hardage, Gao (2013) finds that difficult-to-see subtle structural details are better delineated by higher-frequency wavelets using a spectral probe. In general, the spectral bands that exhibit a lower signal-to-noise ratio should be avoided or at least de-emphasized in seismic attribute analysis. Following this idea, Li and Lu (2014) compute coherence on a suite of spectral components and combine them by using RGB color blending. Not only did this workflow enable an estimate of spectral bands at which the discontinuities occurred, but the results provided better definition of discontinuities amenable to more accurate interpretation. Honorio et al. (2017) use a spectral enhancement differential resolution algorithm to enhance dissimilarities within different frequency bands. They conclude that if an inappropriate scale of observation is used, the target subsurface features of interest may be overlooked. Like Li and Lu (2014), they use RGB color blending of the three most useful frequency bands to visualize the results. Unfortunately, color blending is limited to visualizing only three components at one time.

Chopra and Marfurt (2016) demonstrate how different spectral-decomposition methods provide an effective way of examining the seismic response of stratigraphic geologic features in terms of spectral components. This facilitates a more complete interpretation. In particular, the authors show that an often-overlooked attribute derived during spectral decomposition, called voice components (Marfurt and Matos, 2014), can furnish detailed and crisp information at specific frequencies that are amenable to more accurate interpretation. Coherence-attribute computation performed on spectral voice components within the frequency band of input seismic data could take a lot of computer time and manual effort. Such a problem can be avoided by generating multispectral coherence on input seismic data. Although computationally more intensive than simple broadband coherence, the results yield more accurately defined geologic features and a higher signal-to-noise ratio than those from broadband coherence (Marfurt, 2017; Chopra and Marfurt, 2018, 2019; Li et al., 2018).

For energy-ratio coherence computation, an analysis window consisting of a fixed number of samples in the inline, crossline, and time directions is extracted along structural dip to form a covariance matrix. The first one or two eigenvectors of this matrix are used to compute a principal component filtered version of the data. In this algorithm, the coherence is simply the ratio of the energy of filtered data over the energy of original data in the analysis window. The analysis window is then shifted by one sample at a time in the inline, crossline, and time directions. The process is repeated, resulting in a coherence volume that is ready for interpretation. Multispectral coherence is similar, except the covariance matrices extracted using the same dip magnitude and azimuth are computed for each spectral band and summed prior to principal component filtering (Marfurt, 2017).

In this work, we extend the concept of multispectral computation to dip and azimuth determination and find interesting and encouraging results.

[1]TGS, Calgary, Canada. E-mail: satinder.chopra@tgs.com.
[2]University of Oklahoma, Norman, Oklahoma, USA. E-mail: kmarfurt@ou.edu.

Dip/azimuth computation

There are various ways to estimate volumetric dip and azimuth. The most popular use complex trace analysis, discrete semblance scans, and gradient structure tensor (GST) methods (Chopra and Marfurt, 2007). Of these, the latter two are most widely used in applications such as coherence and curvature computation, edge-preserved smoothing, and structure-oriented filtering. In general, semblance-based algorithms for dip estimation provide slightly better lateral resolution than GST-based algorithms (Bakker, 2003). The latter provide slightly better angular resolution. We discuss the implementation of a GST-based algorithm for computation of multispectral dip components and demonstrate the value addition that accrues in the coherence and curvature attribute computations.

The GST method entails the following steps:

1) The gradient or derivative of the seismic amplitude is computed in each of the three Cartesian directions.
2) A GST is constructed at each grid point within the analysis window by computing the cross correlation and autocorrelation of the three gradient components. The GST matrix so constructed can be augmented with the addition of its Hilbert transform or by following the Luo et al. (2006) approach and computing the GST as weighted derivatives on instantaneous phase.
3) To determine the direction of maximum change, the GST is decomposed into eigenvectors and eigenvalues. Since the GST quantifies the 3D change in amplitude, its first eigenvector provides an estimate of the normal to hypothesized reflector. The apparent dips, p and q measured in m/m (or ft/ft), are given as (Marfurt and Rich, 2010):

$$p = \frac{v_{1x}}{v_{1z}} \tag{1}$$

and

$$q = \frac{v_{1y}}{v_{1z}}. \tag{2}$$

The dip magnitude and dip azimuth can then be computed:

$$\text{dip magnitude} = \sqrt{p^2 + q^2} \tag{3}$$

and

$$\text{dip azimuth} = \text{ATAN2}(q,p). \tag{4}$$

Multispectral dip/azimuth computation

The dip computations themselves can be improved by using different voice components within the spectral band of the input seismic data. As stated earlier, for the GST estimates of dip, the first eigenvector is the normal to a plane that best represents the data in the analysis window. This algorithm is modified by computing a GST for each spectral voice component and summing the results prior to computing the first eigenvector (normal to dip). We refer to the dip magnitude and dip azimuth for each spectral voice component within the spectral band of the input seismic data as "multispectral dips."

Coherence should always be computed along structural dip. In the presence of a gently dipping structure, coherence computed along time slices perceives slightly misaligned seismic events, giving rise to long wavelength smeared anomalies that exhibit shaded illumination. In the presence of a more steeply dipping structure, coherence computed along time slices results in short-wavelength low-coherence artifacts that follow structural contours and overprint the geologic anomalies of interest. Applying overlapping Kuwahara windows further improves the resolution of dip (Marfurt, 2006). In this construct, we output dip from the window that exhibits the lowest chaos, resulting in the dip estimate of reflectors adjacent to a fault rather than a smeared dip estimate averaged across a fault. The multispectral dip estimation is yet another incremental improvement to this suite of tools that results in high lateral resolution.

Application of multispectral dip/azimuth for coherence computation

Dip is a vector. Computationally, dip vectors are comprised of inline and crossline components (p and q in equations 1 and 2). Most interpreters prefer to display the dip vector as separate or corendered dip azimuth and dip magnitude components using equations 3 and 4.

In Figure 1, we show a stratal slice 94 ms below a seismic marker from a survey acquired in Alberta through the inline dip components p computed the traditional way (Figure 1a) and computed using our multispectral dip algorithm (Figure 1b). The east–west inline dip component accentuates north–south-trending events. We identify prominent lineaments with arrows at end points on both displays and note an improvement not only in continuity and lateral resolution, but also in the range of dip values. Both computations were done using a nine 3 trace × 3 trace × 20 ms analysis overlapping Kuwahara windows. Figure 2b shows the corresponding results on the north–south crossline dip component q, which, as expected, accentuates east–west-dipping events. These east–west anomalies appear more continuous and less smeared on the multispectral dip results.

In Figures 3 and 4, we show a similar comparison of most positive curvature (short wavelength) and an overlay of most negative curvature (short wavelength) using transparency over the most positive curvature (short wavelength) display. We notice more focused lineaments and swarms of lineaments on the curvature attributes computed with the use of multispectral dips, as indicated with arrows.

Finally, we draw comparisons between broadband and multispectral energy-ratio coherence displays, as shown in Figures 5 and 6, again without and with the use of multispectral dip components, respectively. Individual lineaments are indicated with arrows. Notice the higher signal-to-noise ratio and better continuity definition of the lineaments after using multispectral dip components in the two coherence displays.

Conclusions

As seen in the examples cited earlier, attributes such as inline dip, crossline dip, dip magnitude, dip azimuth, broadband

DOI:10.1190/tle39080593.1

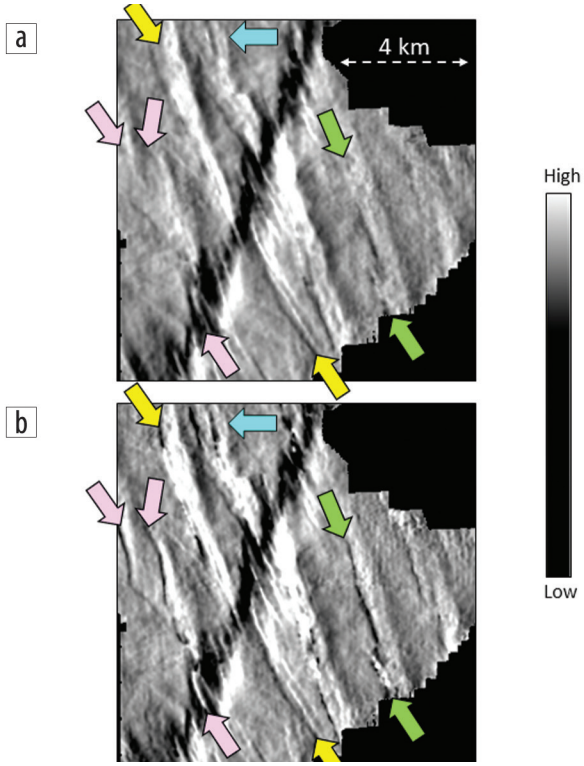

Figure 1. Stratal slice from inline dip volume 94 ms below a marker, when multispectral dips were (a) not used and (b) used in the computation. Most of the lineaments are better defined after the use of multispectral dips, but the ones indicated with pink and green arrows stand out more.

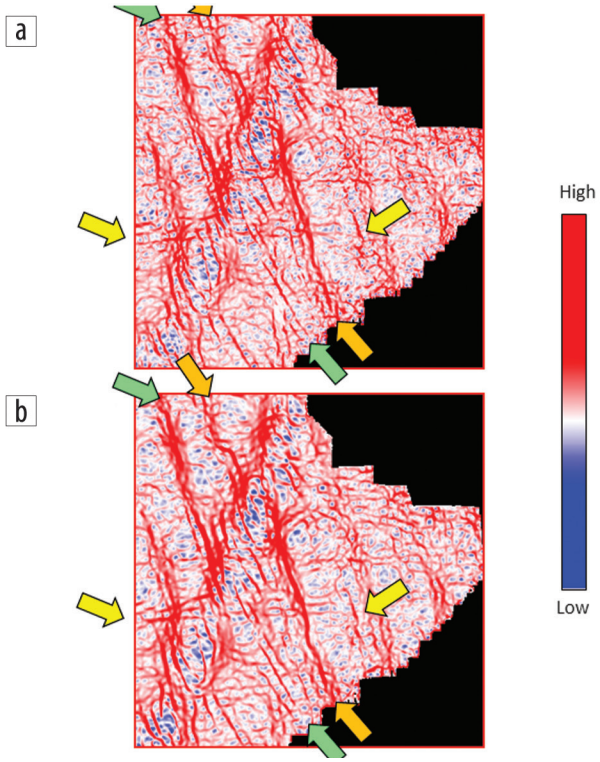

Figure 3. Stratal slice from most positive (short-wavelength) volume 94 ms below a marker, when multispectral dips were (a) not used and (b) used in the computation. While comparing the individual lineaments (marked with arrows), their enhanced definition is noticed in terms of intensity after the use of multispectral dips.

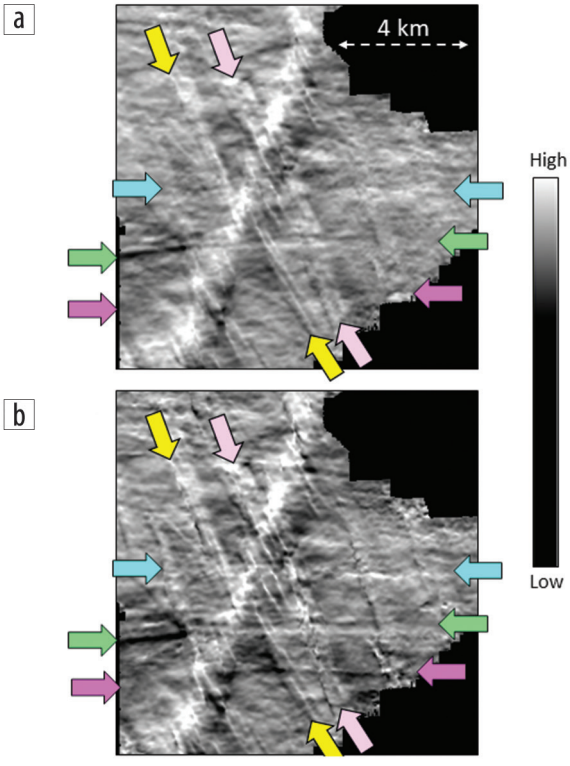

Figure 2. Stratal slice from crossline dip volume 94 ms below a marker, when multispectral dips were (a) not used and (b) used in the computation. Notice how the lineaments indicated with green, magenta, and pink arrows are particularly improved with the use of multispectral dips.

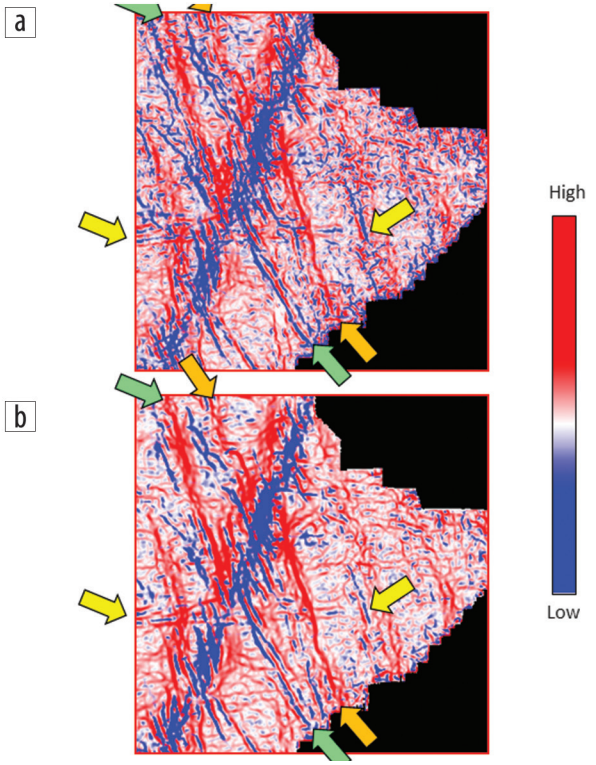

Figure 4. Stratal slice overlay of most negative curvature (short wavelength) using transparency over the most positive curvature (short wavelength) display 94 ms below a marker, when multispectral dips were (a) not used and (b) used in the curvature computation. The lineaments indicated with arrows have enhanced intensity in (b).

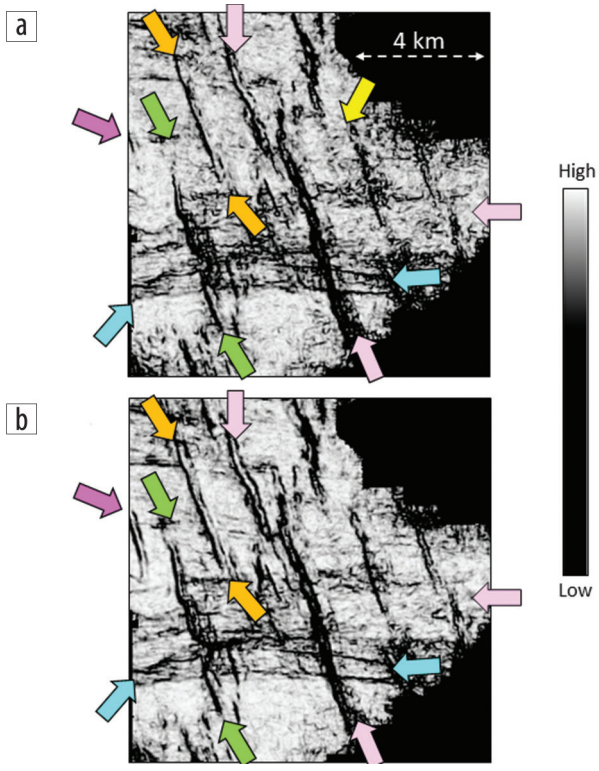

Figure 5. Stratal slice from broadband energy-ratio volume 94 ms below a marker, when multispectral dips were (a) not used and (b) used in the computation. Notice how the different lineaments are better defined and crisp after the use of multispectral dips as shown in (b).

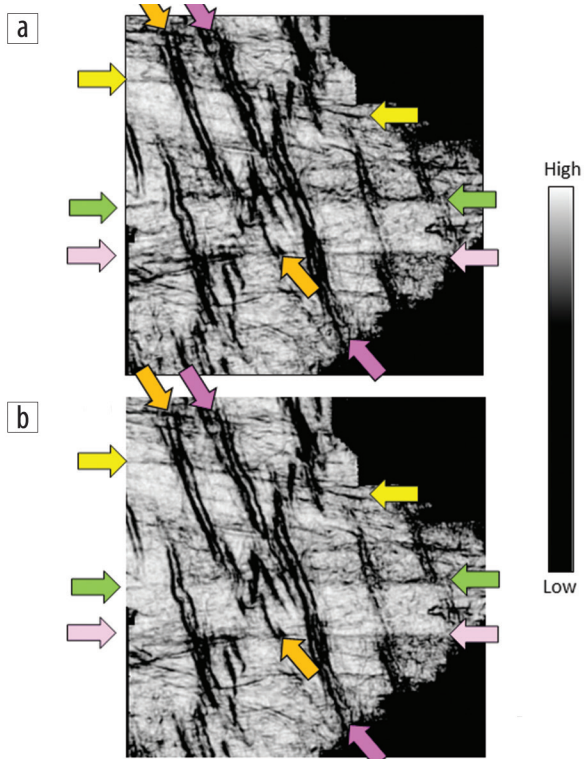

Figure 6. Stratal slice from multispectral energy-ratio volume 94 ms below a marker, when multispectral dips were (a) not used and (b) used in the computation. The lineaments indicated with arrows exhibit crisp definition after the use of multispectral dips in the multispectral energy-ratio computation.

energy-ratio coherence, and multispectral energy-ratio coherence benefit from the use of multispectral dip components in their computation. These benefits include better signal-to-noise ratio, more focused and continuous definition of lineaments, or channel/reef edges (not shown). Consequently, we recommend that multispectral dip components should always be carried out for the generation of such attributes. This will enable more accurate interpretation, which is the bottom line for a seismic interpreter. TLE

Data and materials availability

Data associated with this research are confidential and cannot be released.

Corresponding author: satinder.chopra@tgs.com

References

Bakker, P., 2003, Image structure analysis for seismic interpretation: PhD thesis, Delft University of Technology.

Chopra, S., and K. J. Marfurt, 2007, Seismic attributes for prospect identification and reservoir characterization: SEG.

Chopra, S., and K. J. Marfurt, 2016, Spectral decomposition and spectral balancing of seismic data: The Leading Edge, **35**, no. 2, 176–179, https://doi.org/10.1190/tle35020176.1.

Chopra, S., and K. J. Marfurt, 2018, Multispectral coherence attribute applications: AAPG Explorer, **39**, no. 7.

Chopra, S., and K. J. Marfurt, 2019, Multispectral, multiazimuth, and multioffset coherence attribute applications: Interpretation, **7**, no. 2, SC21–SC32, https://doi.org/10.1190/int-2018-0090.1.

Gao, D., 2013, Wavelet spectral probe for seismic structure interpretation and fracture characterization: A workflow with case studies: Geophysics, **78**, no. 5, O57–O67, https://doi.org/10.1190/geo2012-0427.1.

Hardage, B., 2009, Looking low aids data interpretation: AAPG Explorer, **34**, no. 9.

Honorio, B. C. Z., U. M. C. Correla, M. C. de Matos, and A. C. Vidal, 2017, Similarity attributes from differential resolution components: Interpretation, **5**, no. 1, T65–T73, https://doi.org/10.1190/int-2015-0211.1.

Li, F., and W. Lu, 2014, Coherence attribute at different spectral scales: Interpretation, **2**, no. 1, SA99–SA106, https://doi.org/10.1190/int-2013-0089.1.

Li, F., J. Qi, B. Lyu, and K. J. Marfurt, 2018, Multispectral coherence: Interpretation, **6**, no. 1, T61–T69, https://doi.org/10.1190/int-2017-0112.1.

Luo, Y., Y. E. Wang, N. M. AlBinHassan, and M. N. Alfaraj, 2006, Computation of dips and azimuths with weighted structural tensor approach: Geophysics, **71**, no. 5, V119–V121, https://doi.org/10.1190/1.2235591.

Marfurt, K. J., 2006, Robust estimates of reflector dip and azimuth: Geophysics, **71**, no. 4, 29–40, https://doi.org/10.1190/1.2213049.

Marfurt, K. J., 2017, Interpretational aspects of multispectral coherence: 79th Conference and Exhibition, EAGE, Extended Abstracts, https://doi.org/10.3997/2214-4609.201700528.

Marfurt, K. J., and J. Rich, 2010, Beyond curvature — Volumetric estimation of reflector rotation and convergence: 80th Annual International Meeting, SEG, Expanded Abstracts, 1467–1472, https://doi.org/10.1190/1.3513118.

Marfurt, K., and M. Matos, 2014, Am I blue? Finding the right (spectral) balance: AAPG Explorer, https://explorer.aapg.org/story?articleid=9522, accessed 7 June 2020.